Supplementary Information for Emerging chirality and moiré dynamics in twisted layered material heterostructures

Andrea Silva,[1,2,*] Xiang Gao,[3,4,*] Melisa M. Gianetti,[5,6] Roberto Guerra,[5] Nicola Manini,[5] Andrea Vanossi,[1,2,#] Michael Urbakh,[3,#] Oded Hod[3]

[1] CNR-IOM – Istituto Officina dei Materiali, c/o SISSA, Via Bonomea 265, 34136, Trieste, Italy
[2] International School for Advanced Studies (SISSA), Via Bonomea 265, 34136, Trieste, Italy
[3] School of Chemistry and The Sackler Center for Computational Molecular and Materials Science, Tel Aviv University, Tel Aviv 6997801, Israel
[4] Department of Modern Mechanics, University of Science and Technology of China, Hefei, Anhui 230026, China
[5] Dipartimento di Fisica, Università degli Studi di Milano, Via Celoria 16, 20133 Milano, Italy
[6] Institutt for maskinteknikk og produksjon, NTNU, Richard Birkelands vei 2B, 7034 Trondheim, Norway

[*] These authors contributed equally
[#] Corresponding authors: vanossi@sissa.it, urbakh@tauex.tau.ac.il

1. Comparison between finite angular velocity and quasistatic simulations

In the main text, we presented results of finite angular velocity driving simulations and quasistatic simulations. To evaluate the gradual approach of the former to the latter, Fig. S1 compares the torque traces obtained at angular velocities of $0.05°/\mathrm{ps}$ (solid green) and $0.02°/\mathrm{ps}$ (dashed blue) to the quasistatic trace (dashed-dotted orange). Clearly, the fastest-rotation exhibits strong torque oscillations following slip events. The amplitude of these oscillations reduces as the angular velocity decreases. At $0.02°/\mathrm{ps}$, the deviations between the quasi-static and dynamic simulation results are minor. As a reference to demonstrate the effect of structural flexibility, we report also the torque trace of a fully rigid interface (dotted black). Naturally, it is essential to allow for structural flexibility in order to describe stick-slip dynamics.

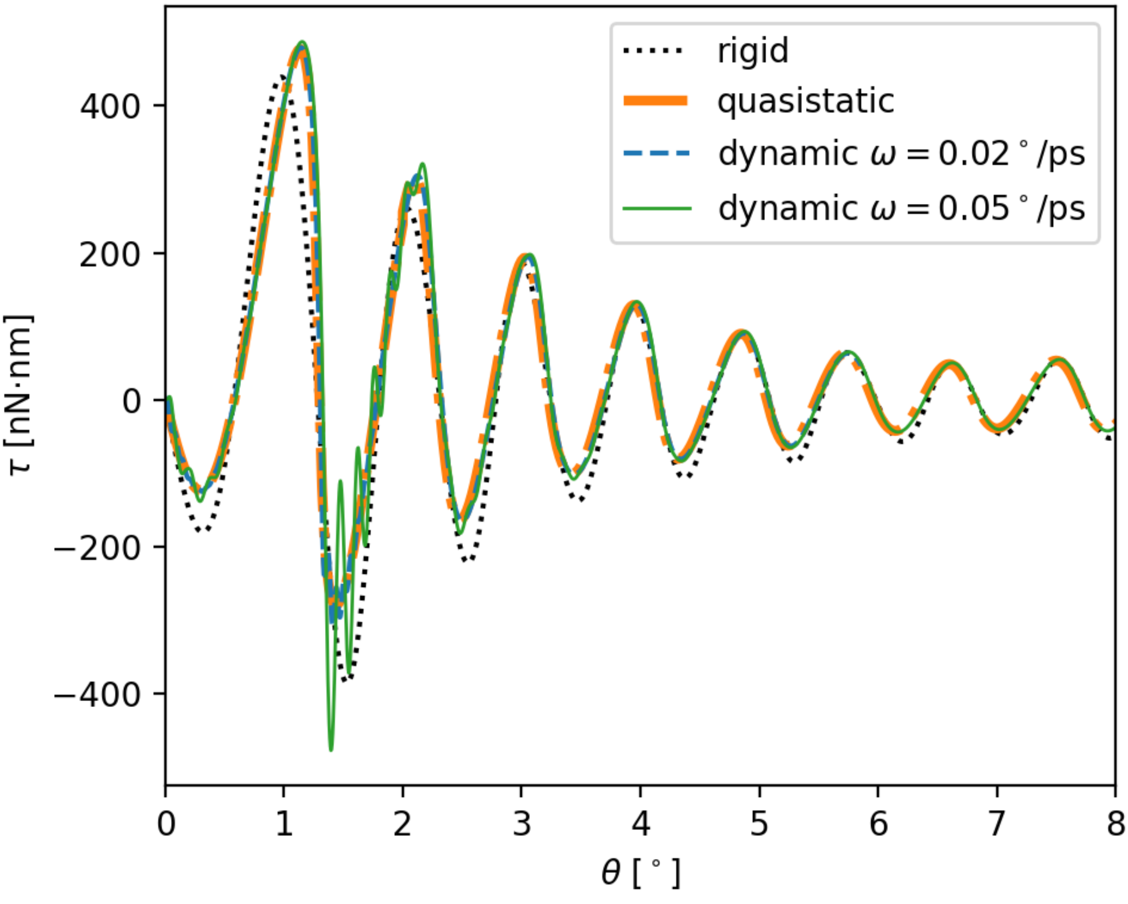

Fig. S1. Effect of angular velocity on the torque traces of flexible 14 nm radius circular graphene/*h*-BN interfaces. The model used herein is the same as that used to produce Fig. 2 of the main text.

2. Angular deformation maps for aligned interfaces

In Fig. 3 of the main text, we presented the angular deformation maps for misaligned configurations of the periodic and finite interfaces, where the latter exhibited chiral patterns. For completeness, we present in Fig. S2 the corresponding angular deformation maps for the aligned case, which exhibit no chiral structures.

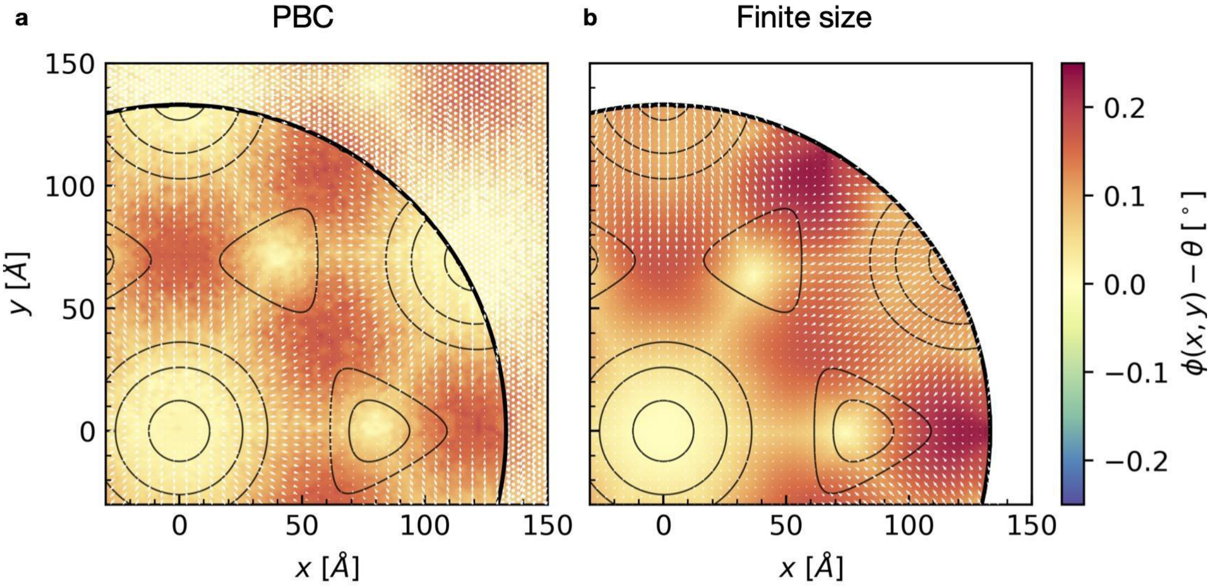

Fig. S2. Local twist angle (see Methods) in aligned ($\theta = 0°$) periodic (a) and finite-size (b) systems. The color scale indicates the deviation between the local twist angle, ϕ and the imposed global twist angle θ. White arrows show the local displacement of the atoms relative to a rigidly rotated system, i.e. the displacement field, magnified by a factor 50 and 22 for panels (a) and (b), respectively. For better visualization, the local angle and displacement vector field are interpolated in the two panels over grids of different densities (700x700 and 140x140 points, respectively). For the laterally periodic system of panel (a) the black arc of radius $R = 14\,\mathrm{nm}$ marks the region corresponding to the finite flake in panel (b); the region outside this circle is shown in transparency for contrast purposes. As a guide to the eye, the black contours highlight the interlayer energy landscape (circles mark minima positions and triangle maxima positions) according to the analytical model presented in the main text.

3. Chiral pattern handedness

In the main text, we presented results of counterclockwise twisting on the heterogeneous circular graphene/*h*-BN interface. For completeness, we compare in Fig. S3 snapshots from quasistatic twisting performed in both the clockwise and counterclockwise senses. Clearly, the two snapshots exhibit mirror image relative deformation maps.

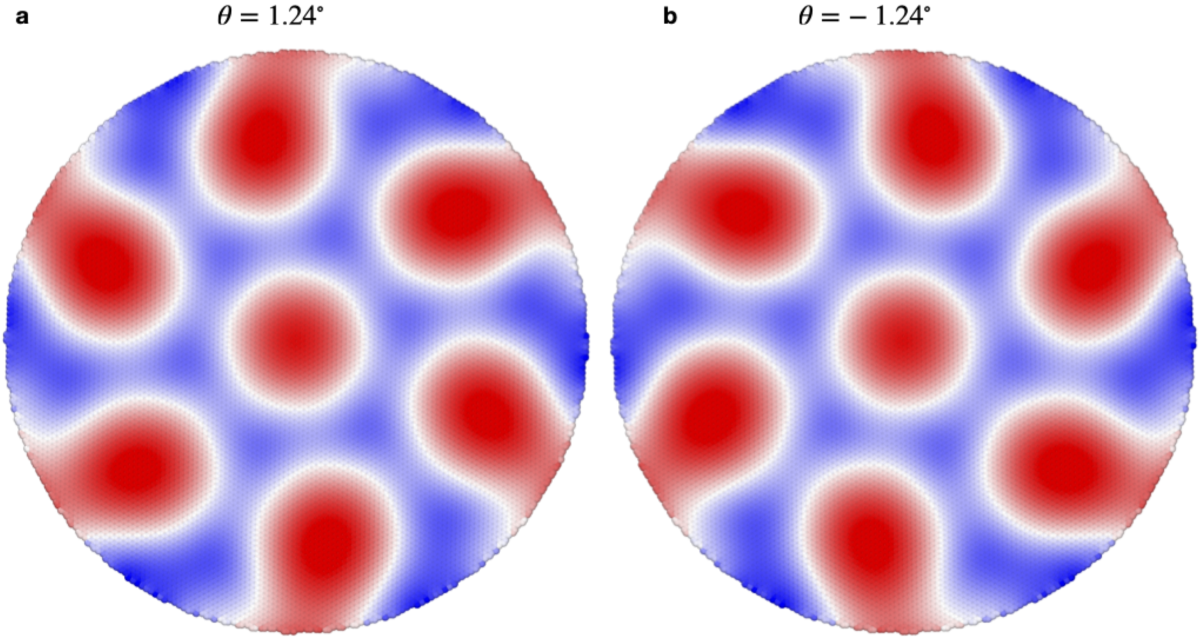

Fig. S3. Chiral pattern handedness. Relative deformation maps obtained for counterclockwise (a) and clockwise (b) quasistatic rotation of $\theta = \pm 1.24^\circ$.

4. Consistency test for the torsional spring model

In order to model systems with thicknesses beyond three layers, while avoiding the explicit and computationally demanding treatment of an extensive number of atoms, we have presented in the main text an alternative approach using torsional springs, whose stiffness can be tuned to mimic different stack thicknesses. To validate this approach, we compare in Fig. S4 the torque trace and retrace diagrams obtained using an explicit 6-layer graphene model (solid blue and orange, respectively) and 3-layers plus springs (dashed red and black, respectively) rotating atop an *h*-BN substrate. Clearly, the spring model captures well the explicit-simulation torque traces.

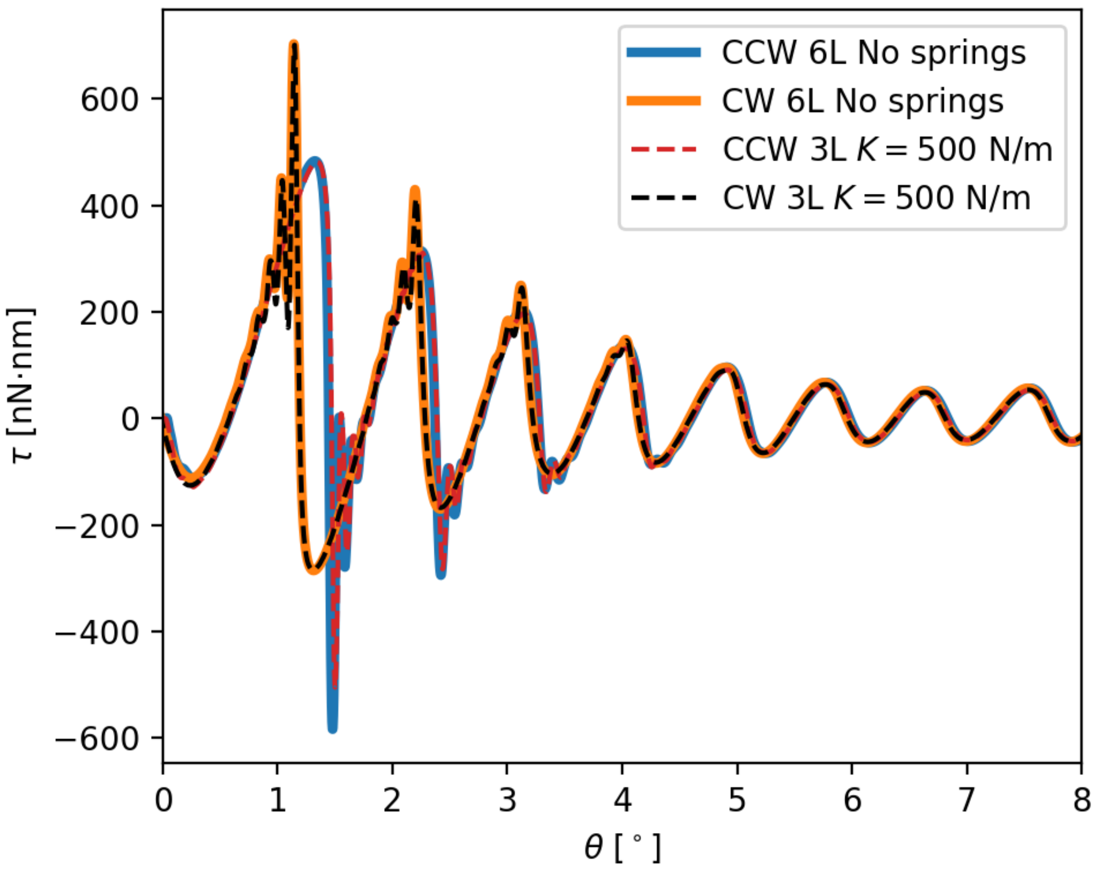

Fig. S4. Torque trace and retrace diagram obtained using an explicit circular ($R = 14$ nm) 6-layer graphene stack (solid blue and orange, respectively) and a 3-layer stack (dashed red and black, respectively) with effective torsional springs rotating atop an *h*-BN substrate. The model system and simulation protocol used herein are the same as those used to produce Fig. 4 of the main text.

5. Details of chirality metrics

The fractional chiral area (*FCA*) definition in Eq. 1 of the main text provides a suitable metric to compare chirality patterns at different twist angles, where the amplitude of the patterns differs. We note, however, that other geometric chirality measures have been introduced in the past to characterize the degree of chirality of any given rigid body.[39,40,41] The main advantage of such measures is that they do not require defining an arbitrary threshold, like in the *FCA* approach. The main deficiency of these measures is that they cannot be applied to continuous fields, such as those obtained when plotting relative deformation maps. This, however, can be remedied by defining a chirality index (CI^{2D}), based on an autocorrelation analysis of a given continuous field with its mirror image. To demonstrate this, we consider a 2D property, $P(\vec{r}) = P(x, y)$, and its mirror image $M(\vec{r}; \alpha)$, rotated at some angle α, which are both integrable ($P \in L^1(\mathbb{R}^2)$) and square integrable ($P \in L^2(\mathbb{R}^2)$). The CI is defined using Pearson's cross-correlation function, as follows:

$$CI^{2D} = \min_{\alpha} \frac{1}{2}\left[1 - \frac{\int d\vec{r}\,(P(\vec{r}) - \bar{P}\,)(M(\vec{r};\alpha) - \bar{M})}{\int d\vec{r}\,|P(\vec{r}) - \bar{P}|^2}\right] \tag{S1}$$

where $\bar{P} = \bar{M}$ denotes the average map value. With this definition, the *CI* obtains a minimal value of $CI^{2D} = 0$ if the map is achiral, an intermediate value of $CI^{2D} = 0.5$ when the map and its mirror image are completely uncorrelated, and a maximal value of $CI^{2D} = 1$ when the map and its mirror image are anti-correlated. Notably, any value in the range $1 \geq CI^{2D} > 0$ signifies a chiral pattern. In practice, in the context of the present paper, for any given twist angle θ, one should consider the relative/angular deformation map of the interfacial graphene layer, interpolate it on a 2D Cartesian grid, construct its mirror image (reflection along the yz plane), such that the centers of the circular domains (the original map and its mirror) coincide, rotate the mirror-image map around the vertical z axis crossing the center by an angle α with respect to the x axis, and evaluate the chirality index, while searching for a minimum as a function of α.

We note that if $P(\vec{r})$ is the characteristic function of a subset (i.e., 1 inside the shape and 0 outside of it), then the definition in Eq. (S1) coincides with the chiral coefficient defined in Eq. 25 of Ref. 40. The definition in Ref. 40 is also related to other chirality measures based on symmetry groups[41] or on inter-set distances in metric spaces[39] as they all deal with characteristic functions of sets and not with patterns defined by continuous functions as our CI^{2D} definition.

Two examples of how the CI^{2D} protocol works for an achiral and a chiral pattern are reported in Figs. S5 and S6, respectively. In Fig. S5a-c, we present an achiral 2D map, and its mirror image rotated by $\alpha = 108°$ and $180°$, respectively. Fig. S5d-e present the integrand of Eq. S1, at those two angles. Clearly, at an angle of $108°$ the integrand gives an asymmetric map that integrates to some finite value, whereas at an angle of $180°$ the integrand vanishes throughout space, indicating perfect correlation (and overlap) between the original map and its mirror image. Integrating the maps at each angle α yields the blue line in Fig. S5h, and the minimum value of this curve as a function of α yields $CI^{2D} = FCA\ = 0$ (obtained at $\alpha = 180°$), indicating an achiral map. Fig. S6 reports a similar analysis for a chiral pattern, yielding a $CI^{2D} > 0$ and $FCA > 0$. While the CI^{2D} analysis is intuitive and completely black-boxified, it is incapable of a comparative analysis of the chirality of structures of different amplitudes, such as those obtained for different twist angles. The reason for this is that Pearson's autocorrelation analysis uses the original map itself as normalization, which in our case depends on the twist angle. Such a twist-angle-dependent normalization prevents a consistent comparison. This is the reason why we opt to use in the main text the chiral area approach, which avoids this kind of twist angle dependent normalization. Notably, a good qualitative agreement between the CI^{2D} and the FCA approach is obtained, as shown by the integrand maps (Figs. S5d-g and S6d-g), and by the minimization curves (blue and orange lines in Figs. S5h and S6h). This is also reflected in Fig. S7, where the *FCA* (dashed blue line) and CI^{2D} (solid orange line) of the deformation maps are plotted as a function of twist angle, θ, for the *R* = 14 nm model system used to plot Fig. 2 of the main text. While the peak positions in the two curves seem to match, the figure exemplifies well how the twist angle dependent normalization of the CI^{2D} makes it impossible to compare the degree of chirality of the deformation maps corresponding to different twist angles.

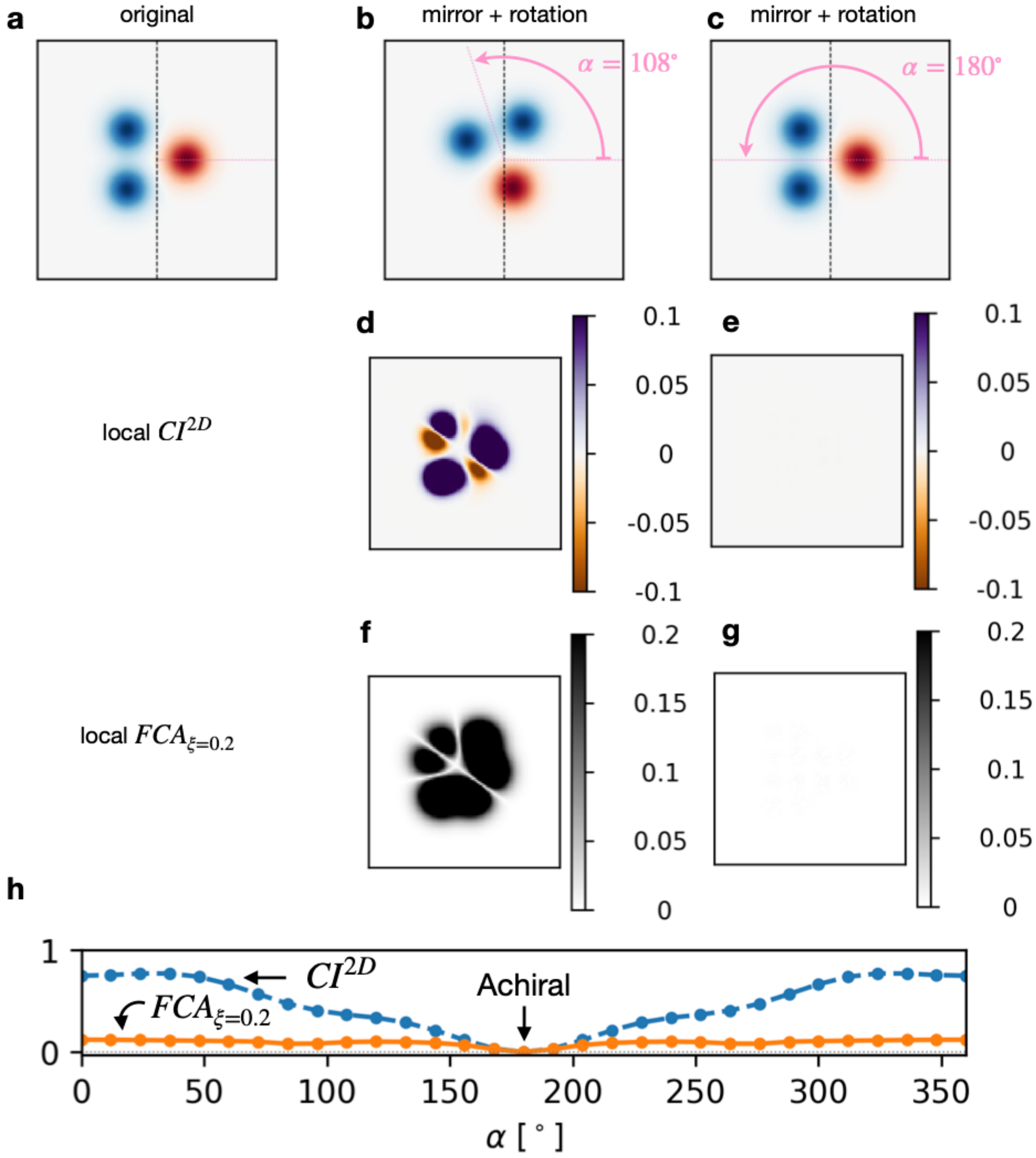

Fig. S5. Example of FCA and CI^{2D} metrics on an achiral pattern. An achiral 2D map (a) and its mirror images rotated by $\alpha = 108°$ (b) and $180°$ (c). (d,e) The local CI^{2D} (i.e. the integrand of Eq. S1) at those two angles, respectively. (f,g) The local FCA (i.e. the integrand of Eq. 1 in the main text) at those two angles, respectively. (h) The CI^{2D} (blue line) and FCA (orange line) as a function of the rotation angle α. The value $CI^{2D} = FCA = 0$, obtained at $\alpha = 180°$, indicates an achiral map.

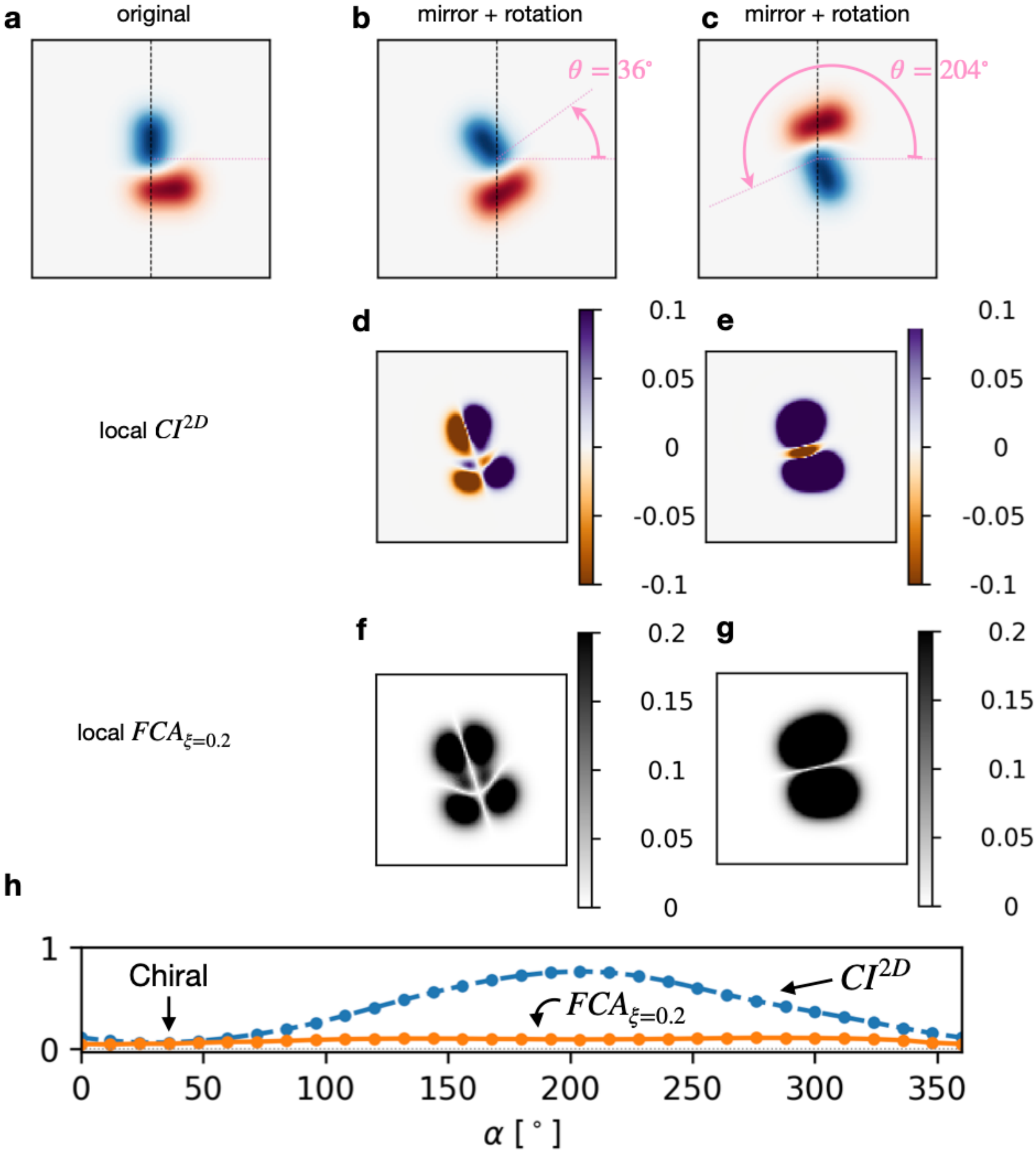

Fig. S6. Example of FCA and CI^{2D} metrics on an chiral pattern. A chiral 2D map (a) and its mirror images rotated by $\alpha = 36°$ (b) and $204°$ (c). (d,e) The local CI^{2D} (i.e. the integrand of Eq. S1) at those two angles, respectively. (f,g) The local FCA (i.e. the integrand of Eq. 1 in the main text) at those two angles, respectively. (h) The CI^{2D} (blue line) and FCA (orange line) as a function of the rotation angle α. The values $CI^{2D} = 0.06$ and $FCA = 0.05$, obtained at $\alpha = 36°$, indicate a chiral map.

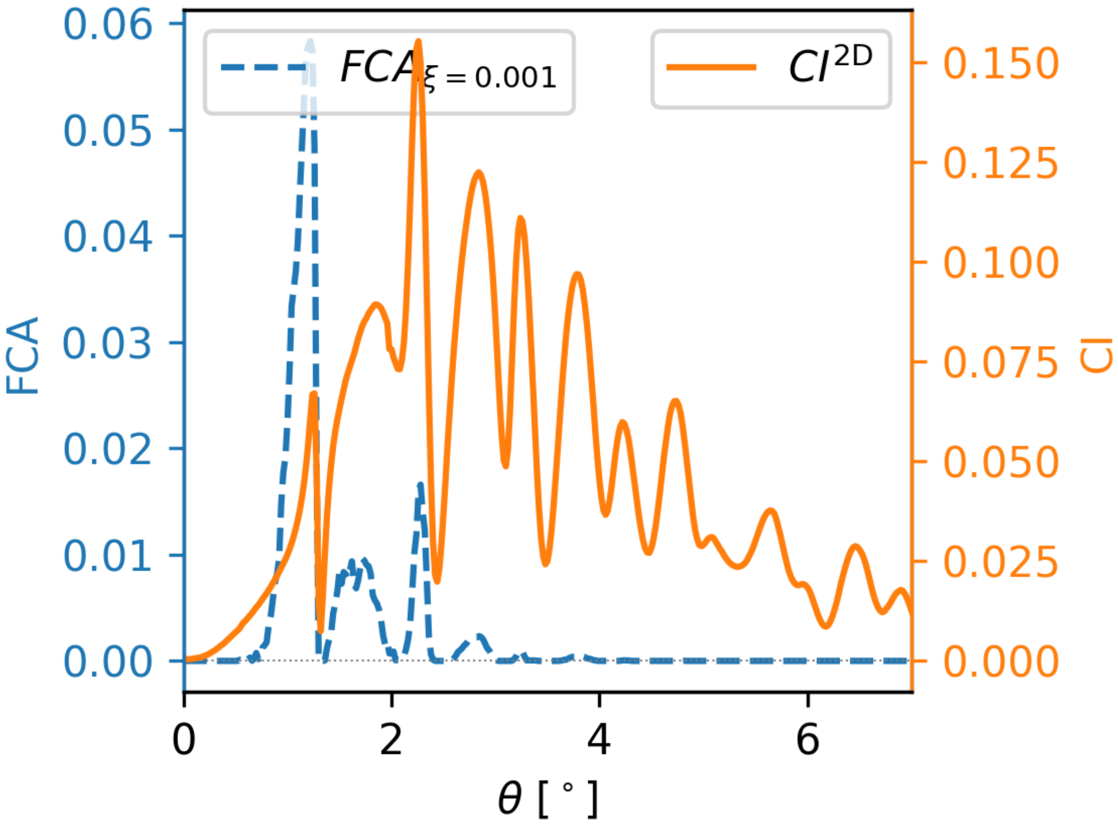

Fig. S7. Comparison between CI^{2D} (solid orange line, right axis) and FCA (dashed blue line, left axis) analyses of the twist angle dependent relative deformation map for the $R = 14\ \mathrm{nm}$ model system used to plot Fig. 2 of the main text. The threshold value used for the FCA analysis is $\xi = 0.001$.

6. Robustness of the chirality effect against contact dimensions

In Fig. 2 of the main text, we presented chirality analysis based on quasi-static simulations for a flake of radius of $R = 14\ \mathrm{nm}$. To demonstrate that the effect is not limited to that specific contact size, we repeated a few of those simulations for a graphene/*h*-BN contact of $R = 21\ \mathrm{nm}$. Comparing Fig. S8 with Fig. 2, the same qualitative behavior is observed, with expected shifts in the positions of the chiral/achiral angles.

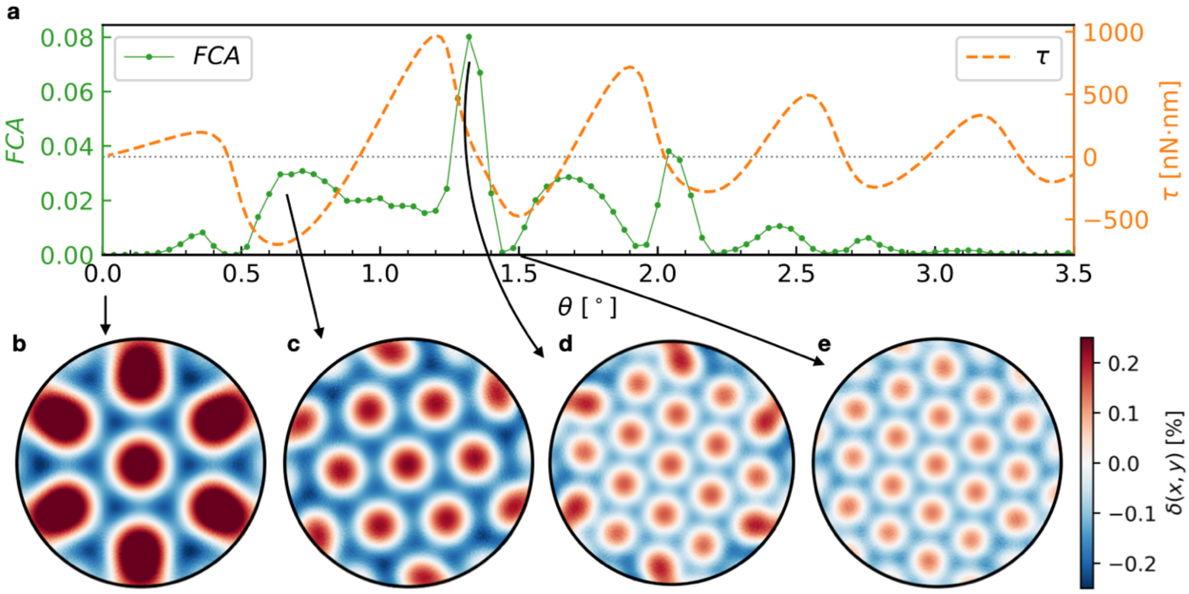

Fig. S8. Chirality fingerprint in the relative deformation map of the $R = 21\ \mathrm{nm}$ tri-layer graphene/*h*-BN contact. Quasistatic twisting leads to elastic deformations of the interface, characterized by a chiral pattern. (a) fractional chiral area $FCA_{\xi=0.001}(\theta)$ (solid green, left axis) and torque (dashed orange, right axis) as a function of twist angle. In the lower panels, the strain patterns correspond to the aligned configuration (b), two FCA maxima (c,d) and one minimum (e). The color code expresses the strain field as reported by the color bar on the bottom right.

7. Single-layer limit

In the main text, we presented results for multi-layer contacts. To verify if the rotational stick-slip dynamics and the chirality persist down to the monolayer limit we repeat some of the calculations for single-layer graphene flakes deposed on *h*-BN. Imposing a twist angle directly to a single unconstrained graphene layer and measuring the resulting torque is ill-defined, as the result depends on the applied twist protocol. Hence, we tackle this ambiguity by simulating two extreme cases: an angular twist applied to a rigid region at the center of the flexible flake, or the same twist applied to a rigid-edge rim. In both protocols chiral/achiral transitions are observed, as shown in Figs. S9 and S10. Since the emergence of chiral patterns is associated with edge pinning effects, for rigid edge-simulations this result is somewhat surprising. Nonetheless, we attribute this behavior in the rigid edge case to the elasticity of the rim of the central flexible region in the vicinity of the thin rigid outskirt of the flake.

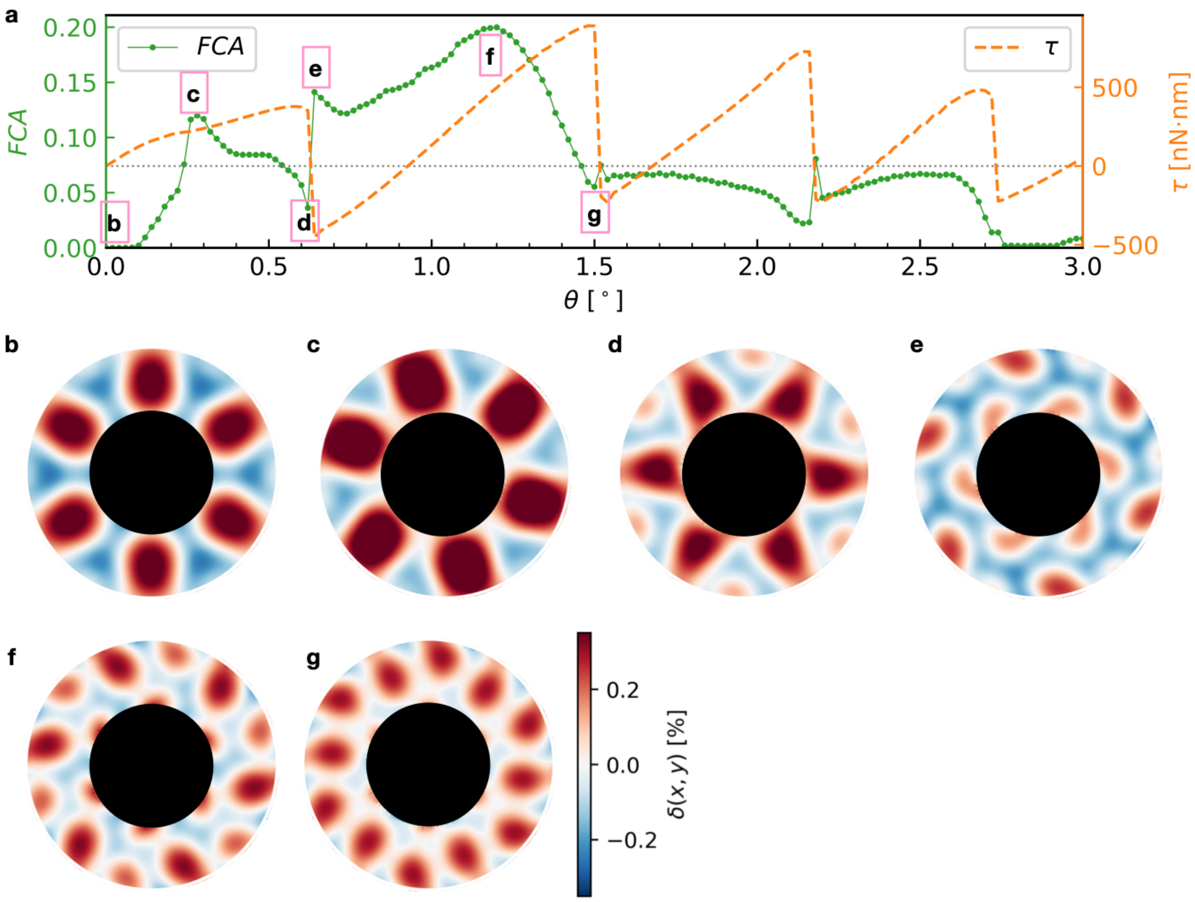

Fig. S9. Chirality fingerprint in the elastic displacement map of an $R = 21\ \mathrm{nm}$ single-layer graphene/*h*-BN contact, where twist is applied to the rigid central region (marked in black in panels b-g). Quasistatic twisting leads to elastic deformations of the interface, characterized by a chiral pattern. (a) chiral area $FCA_{\xi=0.001}(\theta)$ (solid green, left axis) and torque (dashed orange, right axis) as a function of the twist angle. Panels b-f show the strain patterns corresponding to twist angles of $\theta = 0°, 0.28°, 0.62°, 0.64°, 1.2°, 1.5°$, marked in panel a. The color code expresses the strain field as reported by the color bar on the bottom right.

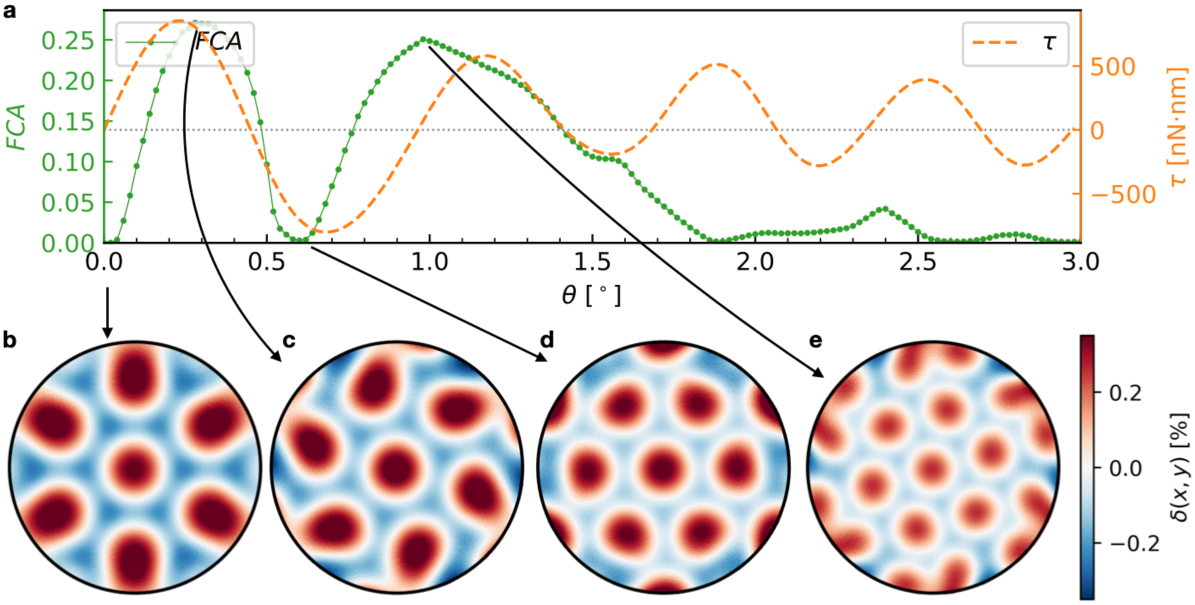

Fig. S10. Chirality fingerprint in the elastic displacement map of the $R = 21\ \mathrm{nm}$ single-layer graphene/*h*-BN contact with fixed rim edge region (marked in black)**.** Quasistatic twisting leads to elastic deformations of the interface, characterized by a chiral pattern. (a) chiral area $FCA_{\xi=0.001}(\theta)$ (solid green, left axis) and torque (dashed orange, right axis) as a function of twist angle. In the lower panels, the strain patterns correspond to the aligned configuration (b), two FCA maxima (c,e) and one minimum (d). The color code expresses the relative deformation as reported by the color bar on the botom right.

Fig. S11 reports the comparison of the torque traces for these two twisting protocols. While the torque values are in the same range, we observe quite different elastic responses of the two models: when the twist is applied to the rigid central region, a strong stick-slip instability is observed (orange circles in Fig. S11). Conversely, when applying the twist to the rigid rim edge (see blue squares in Fig. S11), the flake exhibits little global deformations, thus producing a smooth torque profile with no indication of instability. This further supports our claim that stick-slip twisting in this system originates from edge pinning.

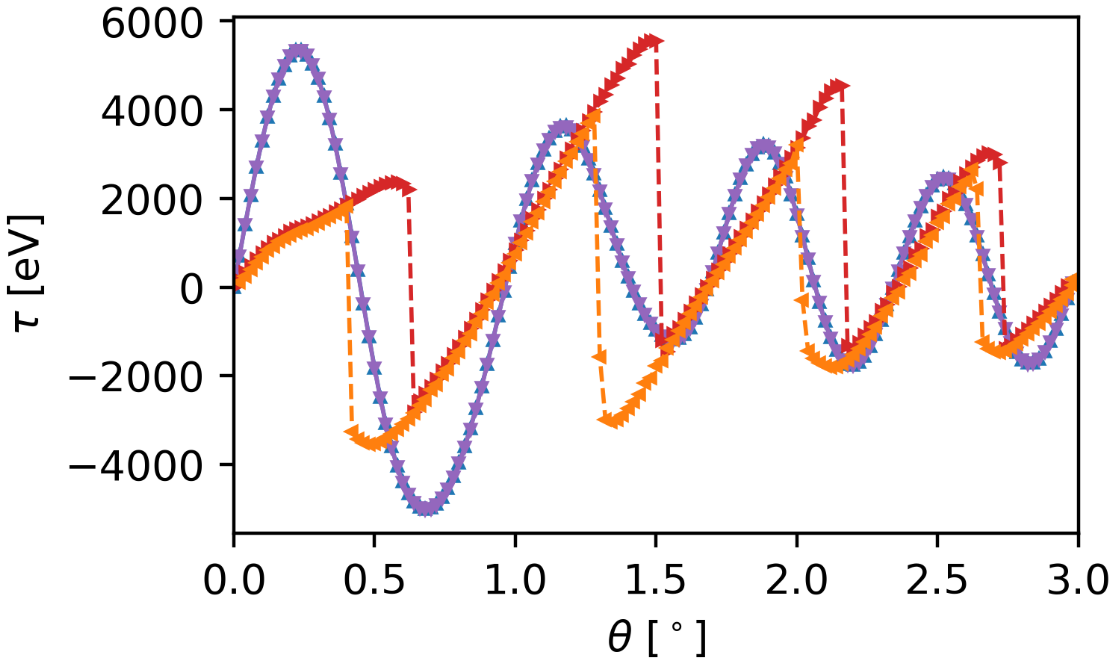

Fig.

Fig. S11. Twisted single-layer graphene flake over an *h*-NB substrate. Torque trace and retrace as a function of the twisting angle θ of the rigid center (trace in red and retrace in orange, see Fig. S9) or of rigid edge (trace in blue and retrace in purple, see Fig. S10). Stick-slip motion and hysteresis are seen in the former case, whereas smooth-sliding with no evidence of hysteresis is observed for the latter case.

8. Chirality in homogeneous graphitic interfaces

In the main text, we have presented results of stick-slip/smooth-sliding and chiral/achiral transitions upon twisting of circular heterojunctions of graphene and *h*-BN. To demonstrate that this effect is of general nature and not limited to this specific interface, we performed similar simulations for homogeneous graphitic interfaces. As can be seen in Figs. S12 and S13, the same qualitative behavior is obtained for both the optimal and the worst initial stacking modes. For the commensurate AB stacked case, the first dynamic slip event is very vigorous, resulting in dynamic reverberations in the torque trace. The AA stacked system exhibits a behavior which is very similar to the one demonstrated for the heterojunction.

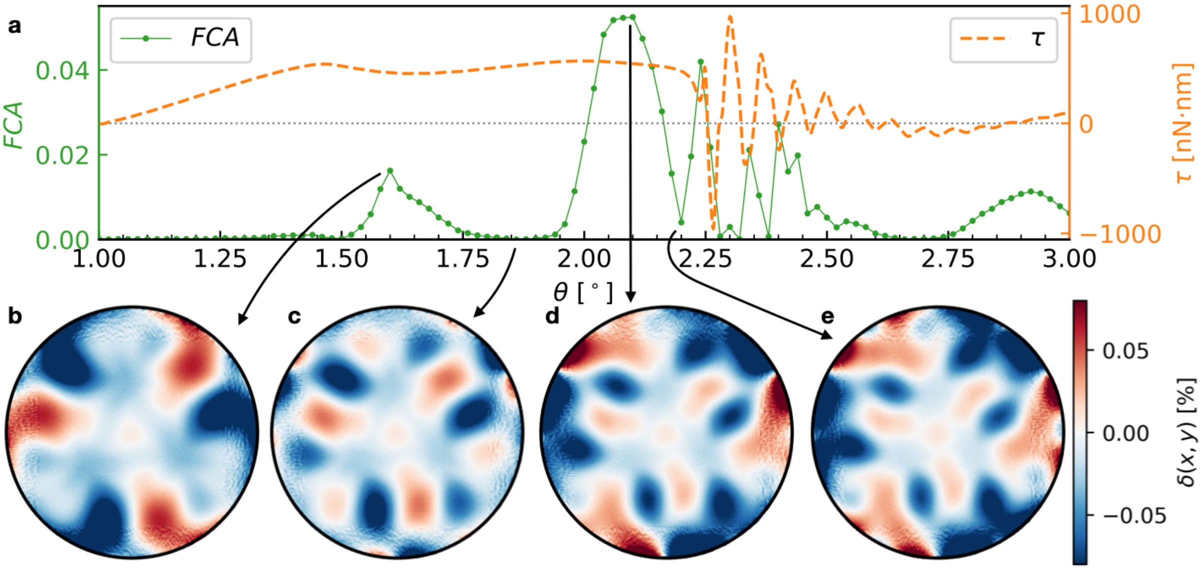

Fig. S12. Chirality fingerprint in the elastic displacement map of the initially AB stacked $R = 14\ \mathrm{nm}$ trilayer graphene/trilayer graphene contact. Dynamic twisting at $\omega = 0.02\ °/\mathrm{ps}$ leads to elastic deformations of the interface, characterized by a chiral pattern. (a) chiral area $FCA_{\xi=0.001}(\theta)$ (solid green, left axis) and torque (dashed orange, right axis) as a function of twist angle, starting from $\theta = 1\ °$. In the lower panels, the strain patterns correspond to two FCA maxima (b,d) and two minima (c,e). The color code expresses the relative deformation as reported by the color bar on the bottom right.

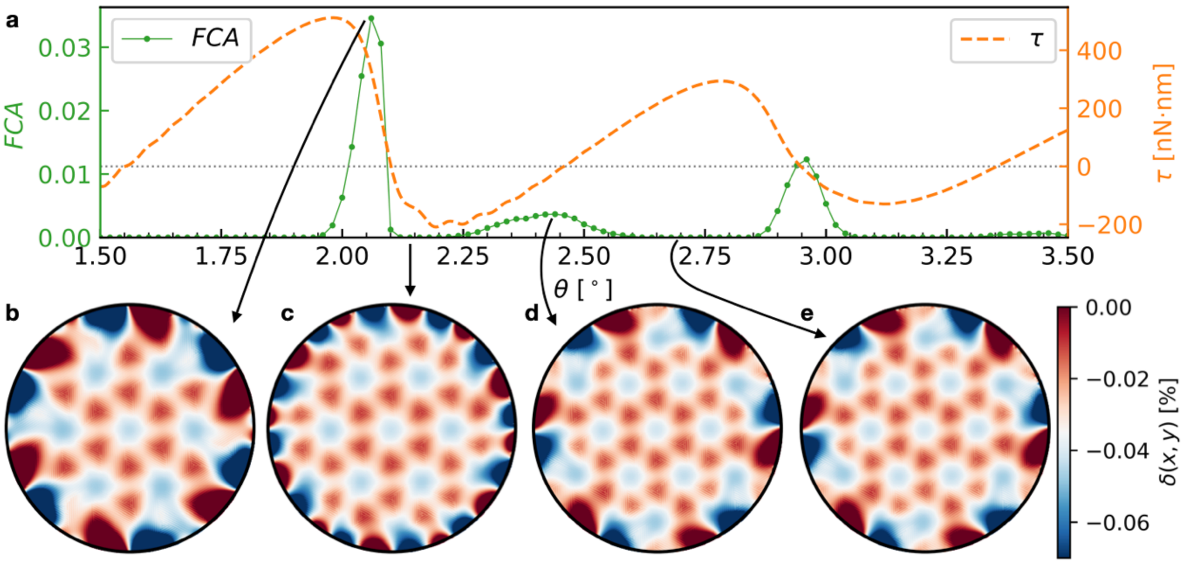

Fig. S13. Chirality fingerprint in the elastic displacement map of the initially AA stacked $R = 14\ \mathrm{nm}$ trilayer graphene/tri-layer graphene contact**.** Dynamic twisting leads to elastic deformations of the interface, characterized by a chiral pattern. (a) chiral area $FCA_{\xi=0.001}(\theta)$ (solid green, left axis) and torque (dashed orange, right axis) as a function of twist angle, starting from $\theta = 1.5\,°$. (b-e) the strain patterns corresponding to two FCA maxima (b,d) and two minima (c,e). The color code expresses the relative deformation as reported by the color bar on the bottom right.

9. Energy as a function of twist angle

As discussed in the main text, the FCA peaks correlate with the interfacial angular stiffness $(d\tau/d\theta)$ maxima and minima, which occur when the system deforms to oppose rotation or when it jumps towards the next angular energy minimum, respectively. To demonstrate this point, we report in Fig. S14 the total energy as a function of twist angle for the trilayer graphene/*h*-BN circular contact of radius $R = 14\ \mathrm{nm}$. Clearly, the FCA peaks near (local) energy minima and maxima.

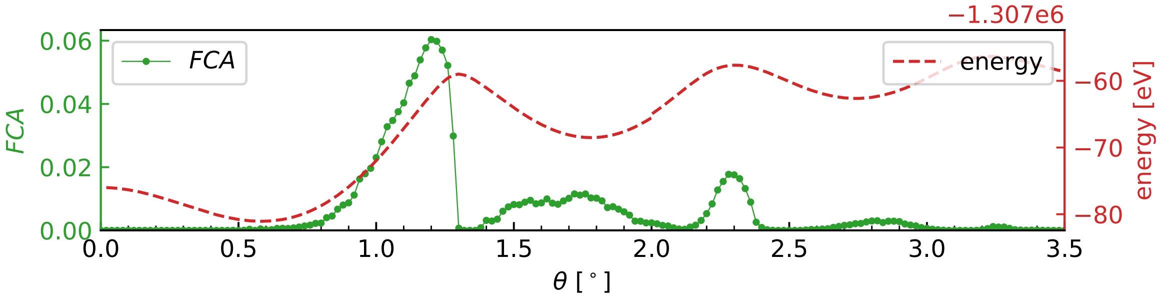

Fig. S14 Energy as a function of twist angle for the $R = 14\ \mathrm{nm}$ trilayer graphene/*h*-BN contact. The chiral area $FCA_{\xi=0.001}(\theta)$ (solid green, left axis) and energy (dashed red, right axis) as a function of twist angle, starting from $\theta = 0\,°$.

10. Chirality in dynamic simulations

To show that the chirality fingerprint is qualitatively the same in the quasistatic and dynamic simulations, Fig. S15 reports the FCA and the torque for the same system studied quasistatically in Fig. 2 of the main text, now under dynamic twisting at constant angular velocity $\omega = 0.02$ °/ps.

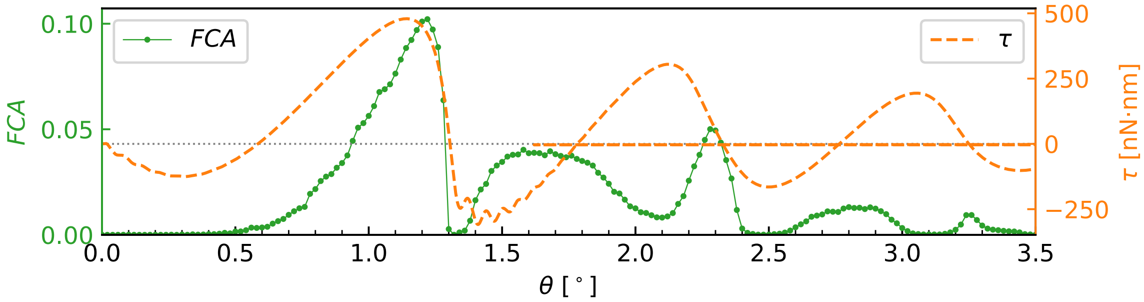

Fig. S15. Chirality fingerprint in the elastic displacement map of the $R = 14$ nm single-layer graphene/*h*-BN contact**.** Dynamic twisting at $\omega = 0.02$ °/ps leads to elastic deformations of the interface, characterized by a chiral pattern. (a) chiral area $FCA_{\xi=0.001}(\theta)$ (solid green, left axis) and torque (dashed orange, right axis) as a function of twist angle.

11. Details of the rigid rotation stage and lateral springs

In the main text (Fig. 4a), a schematic representation of the molecular dynamics simulation setup was presented. To show in more details the connection scheme between the rigidly rotating stage and the top layer of the graphitic flake, we provide in Fig. S16 a top view of the system showing the location of the carbon atoms to which the six springs of constant K are connected. These atoms are located at distance R_s from the center of mass of the graphitic flake and are angularly separated by $60°$.

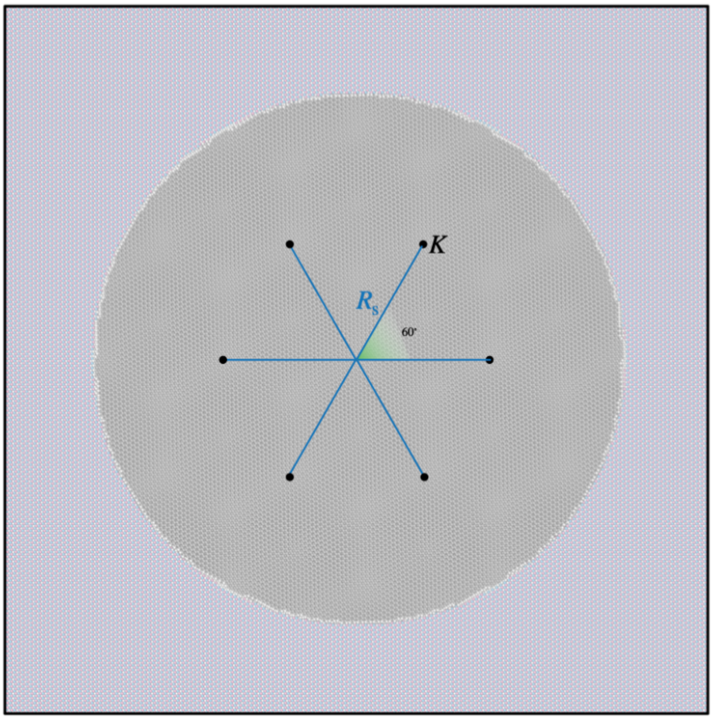

Fig. S16. Top view of the graphitic flake residing atop the *h*-BN substrate, showing the contact points (black circles) of the six springs of constant K, connecting the rigid stage to the top rigid graphene layer. The springs are connected at a distance R_s from the center of mass and separated by $60°$ degrees from each other.

12. Chirality in heterogeneous interface with hexagonal flake

In the main text, we presented the emergence of chirality for a circular flake of radius of $R = 14\ \mathrm{nm}$. To demonstrate that the effect is not limited to that specific contact shape, we performed dynamic twisting simulations at $\omega = 0.02\ °/\mathrm{ps}$ simulations for a hexagonal graphene/*h*-BN contact of apothem $\mathrm{a} = 18.9\ \mathrm{nm}$. Comparing Fig. S17 with the analysis in the main text, the same qualitative behavior is observed: an alternation of chiral and achiral patterns as the twists proceeds.

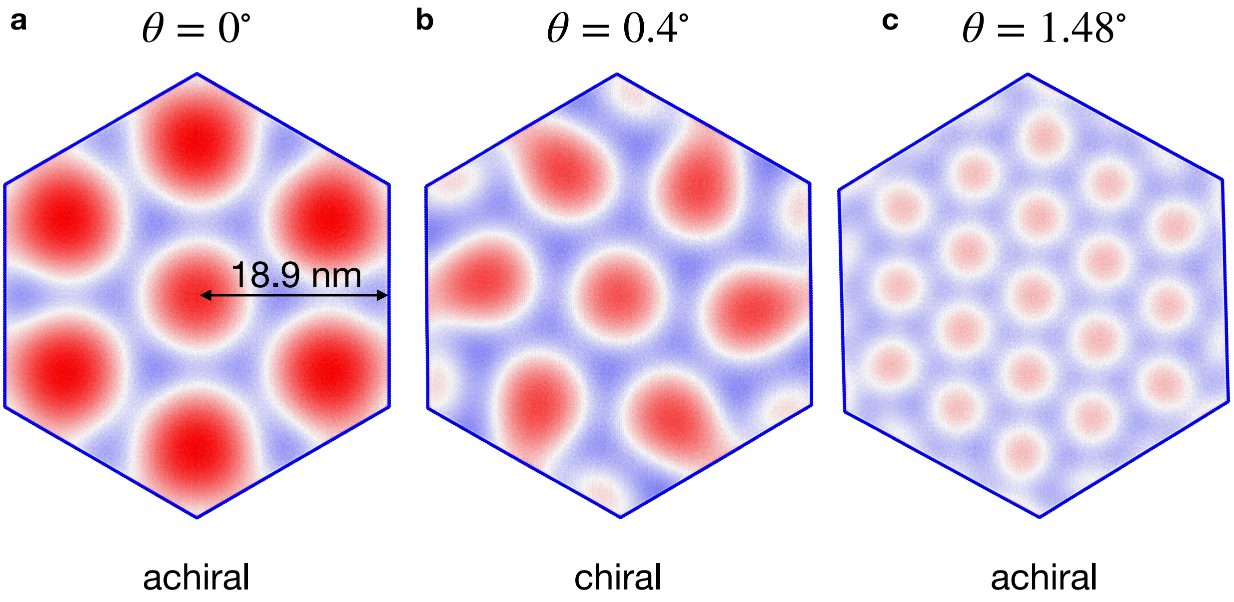

Fig. S17 The strain patterns exhibiting two achiral (a,c) and one chiral (b) configuration at the twist angle indicated above. The color code expresses the relative deformation as reported by the color bar in Fig.2 of the main text.